

Internal waves excited by the Marangoni effect

A. Wierschem,^{1,2} H. Linde,^{1,3} and M. G. Velarde¹

¹Instituto Pluridisciplinar, Paseo Juan XXIII, No. 1, E-28040 Madrid, Spain

²LS Technische Mechanik und Strömungsmechanik, Universität Bayreuth, D-95440 Bayreuth, Germany

³Straße 201 Nr. 6, D-13156 Berlin, Germany

(Received 13 December 1999; revised manuscript received 26 May 2000)

Traveling periodic internal wave trains are generated in liquid layers during the absorption process of a miscible surface-active substance out of the vapor phase. In our nonstationary experimental runs, internal waves are excited by surface waves, which had been previously generated by a surface-tension-gradient-driven instability. The internal wave trains adjust their wave number by an Eckhaus instability. Close to the instability threshold narrow and extended pulses are observed. Furthermore, the wave trains can alter their traveling direction, i.e., one wave train traveling in one direction yields to another train, in general of different wave number, traveling in the opposite direction.

PACS number(s): 47.20.-k, 47.35.+i, 47.55.Hd

I. INTRODUCTION

Internal waves are observed in many geophysical systems like ocean currents, the atmosphere, or magma flows. They are usually generated by a shear-flow instability in the bulk [1–9]. Internal waves can also be generated in an initially motionless fluid by surface shear. This shear, for example, could be produced by a wind blowing over the surface that first generates surface waves [10]. Then these surface waves can transfer their energy to the internal waves. Ball [11] investigated the resonant energy transfer between a pair of surface waves and an internal one, which is likely to be a powerful mechanism. Recently, Rednikov *et al.* showed possible excitation of internal waves due to a Rayleigh-Marangoni instability [12].

Here we report on the generation and evolution of internal waves during the absorption of a miscible surfactant out of the vapor phase by a liquid. There is neither a finite, localized perturbation nor an imposed flow. Along an annular ring channel these internal waves travel as wave trains or as narrow or extended pulses. They show a short-wave instability and they adjust their wave number by an Eckhaus instability. They may also alter their traveling direction.

II. EXPERIMENTAL SYSTEM AND SETUP

A side view of the setup is sketched in Fig. 1. It consists of a cylindrical glass container in which two quartz rings are placed concentrically. The two rings are concentric within 1%. Besides that shown in Fig. 1, another container with an inner ring of 54.25 ± 0.05 mm diameter was used. Its outer

diameter is 74.60 ± 0.05 mm and the height of the quartz-glass rings is 8.85 ± 0.1 mm. The rings are concentric within 3%. They are fixed with the two-component adhesive Araldit® from Ciba-Geigy. Contamination of the liquid by the adhesive or dissolution and aging of the adhesive points has not been observed. The annular gap between the two quartz rings is filled with toluene. The rest of the container is covered with liquid pentane, which has a high vapor pressure at room temperature and a surface tension much lower than toluene. Because the surface level rises due to the absorbed pentane the annular container is not filled brimful. The experiment begins by covering the reservoir with a quartz-glass plate. To maintain atmospheric pressure this plate is not tightly fixed and the enclosure is thus slightly open to the ambient air. The experimental runs are carried out at ambient temperatures between 297.65 and 298.85 K. In addition, we have carried out some experimental runs in the container of 50 mm inner diameter with the reservoir open to the ambient air at temperatures between 299.75 and 300.05 K.

We have chosen toluene as the liquid and pentane as the absorbable and completely miscible surfactant. Property values for the pure substances at atmospheric pressure are given in Table I [13]. The surface tension and viscosity of liquid pentane are much lower than those of liquid toluene. The same holds for the density. This is the key feature for the generation of internal waves as the liquid layer becomes stably stratified due to the absorption of pentane. We also give the refractive index of the fluids in the table. The refractive index of pentane vapor is almost the same as that of air. Accordingly, we expect that optical rays traversing the vapor phase are not deflected. Furthermore, the boiling point of

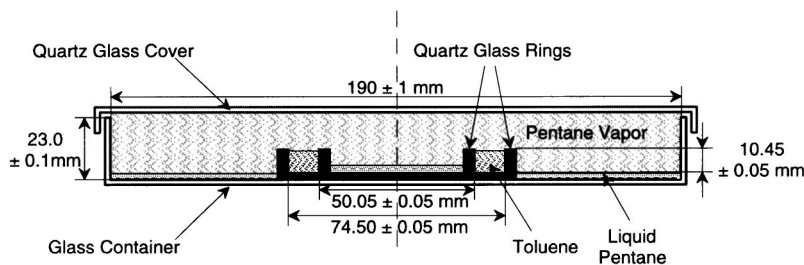


FIG. 1. Side view of the experimental setup: two quartz-glass rings form an annular container which is placed concentrically in a circular reservoir made of glass. The annular ring is filled with toluene and the bottom of the reservoir is covered with liquid pentane. The experiment starts when the reservoir is covered with a quartz-glass plate.

TABLE I. Properties of liquid toluene and liquid pentane [13].

Property	Liquid toluene	Liquid pentane	Pentane gas
Molecular weight u (g/mol)	92.15	72.15	72.15
Boiling point T_B (K)	383.75	309.22	
Density ρ at 293.15 K (g/cm ³)	0.8669	0.6262	
Refraction index n at sodium D line	1.4961	1.3575	1.001 711
Surface tension σ at 298.15 K (mN/m)	27.93	15.49	
Viscosity η at 298.15 K (mPa s)	0.560	0.224	0.006 76

pentane is about 11 K above room temperature at atmospheric pressure. For toluene the corresponding value is higher. Within the range of the experimental runs the effect of temperature on the parameters is low and can be neglected.

A literature value for the diffusion of pentane in air and in liquid toluene has not been found. However, an estimate of its magnitude can be obtained from other data in the literature. The diffusion coefficient for a system of two simple gases is usually about 10^{-5} m²/s. For pentane in air, the model of Wilke and Lee [14] gives 4.2×10^{-6} m²/s with a factor 2 as the expected error. The diffusivity of pentane in toluene can be approximated from the known values of the toluene-heptane and toluene-hexane systems. These systems have diffusion coefficients of 3.72×10^{-9} and 4.21×10^{-9} m²/s, respectively [13]. Thus, by extrapolation the coefficient of pentane in toluene is taken to be about 5×10^{-9} m²/s. The values of the vapor pressure of pentane and toluene have been taken from [13] and [15]. In the temperature range between 296 and 301 K the vapor pressure of pentane increases linearly from 63.0 to 76.1 kPa, taking the form $C_{PV} = -7.065$ (mol) + $0.025\,968$ (mol K⁻¹) T , while that of toluene grows from 3.36 to 4.37 kPa.

As the two components do not react, the density changes linearly with concentration. The viscosity of miscible liquid mixtures η is usually well described by the Kendall-Monroe equation [16], which in our case reads

$$\eta(C_P) = [\eta_P^{1/3} C_P + \eta_T^{1/3} (1 - C_P)]^3, \quad (1)$$

where C_P denotes the pentane concentration, and η_P and η_T are the viscosities of pure pentane and pure toluene, respectively. The surface tension as a function of the concentration at $T=298.15$ K has been measured semiautomatically with a TE 1 C tensiometer by Lauda, using a platinum ring for the stirrup method [17]. The data can be fitted with an exponential-decay function $\sigma = \sigma_0 + \sigma_1 \exp(-C_P/C_{P0})$, with $\sigma_0 = 11.81 \pm 0.21$ mN m⁻¹, $\sigma_1 = 16.24 \pm 0.20$ mN m⁻¹, and $C_{P0} = 0.682 \pm 0.018$ mol. Further details can be found in [17].

The internal waves have been visualized by applying the shadowgraph method. The light coming from a monochromatic light source of 1 mm diameter is collimated to a parallel beam of 100 mm diameter. After traversing the hydrodynamic system from underneath the collimated beam is focused by a lens. Together with a zoom it adjusts the size of the beam arriving at the charge-coupled device (CCD) chip of the camera that records the image. The camera works at a

video frequency of 25 Hz. The images are stored on video tape and subsequently processed by computer.

The surface deformation caused by the waves is detected with a laser beam reflected at the liquid surface. The reflected part of the beam is detected on a recording plane. If the surface at the irradiation spot is deformed, the position of the reflected beam on the recording plane moves. The position of the spot on the plane is recorded by a CCD camera, stored on video tape, and evaluated subsequently by computer. The surface deformation gradient h_x is calculated from the shift of the laser spot on the recording plane and integrated with the phase velocity of the waves that travel underneath the laser beam.

The convective flow has been detected by photochromic flow visualization. It has the advantage over visualization with tracer particles that it does not alter the liquid parameters locally. Unlike use of dyes, the method is suitable for investigations in closed hydrodynamic systems due to the reversible transition. An overview of the method is found in [18]. As photochromic substance we use 1,3,3-trimethylindolino-6-nitrobenzopyrylospiran (TMINBPS) which is completely soluble in toluene. We have mixed amounts of the order of 1:10 000 by volume so that the liquid parameters are barely altered. A small slot is irradiated by a nitrogen laser with a beam diameter in the liquid of about 1 mm. Thereby the photochromic substance in this slot is excited and becomes visible. The diameter of the irradiation column does not change significantly in time. Hence, diffusion of the colored column can be neglected during the measurement. Experiments are conducted with the laser beam traversing the liquid from the side and from above. The displacement of the irradiated line, which corresponds to the Lagrangian flow trajectory, is recorded from the side and also from above in the shadowgraph mode. The measurements are correlated with the shadowgraph visualization. Further details of the experimental methods are given in [17].

III. EXPERIMENTS

A. Temporal evolution

The experiments start by covering the reservoir with a glass plate. Then the vapor concentration of pentane rises rapidly until its stationary value determined by the vapor pressure is achieved. Thus, a strong concentration difference between the vapor phase and the liquid is created. This difference decreases with time due to the absorption of pentane in the liquid, until the pentane surface concentration in the

liquid is the same as in the vapor. At the beginning of this equilibration process surface waves are observed. Since the pentane that is absorbed by the liquid toluene remains in the liquid, the experiment is nonstationary by its nature. Therefore, we first give a survey of the temporal evolution of a typical experimental run, as it is observed with the shadowgraph technique.

During the experimental runs, parameters like the density, the viscosity, and the surface tension change with time. They all depend on the pentane concentration within the liquid. The absolute amount of absorbed pentane is obtained by measuring the height of the surface level as a function of time. We neglect the evaporation of toluene due to its much lower vapor pressure with respect to pentane. The temporal evolution of the pentane absorption rate can be fitted to an exponential-association fit. In the range where internal waves are observed, the vapor has already reached its saturation value and the fit of the absorption rate A_p through the surface of the annular ring simplifies to

$$A_p(t) = \frac{\rho_p}{u_p} \pi(r_o^2 - r_i^2) \frac{h_1}{\tau} \exp\left(-\frac{t}{\tau}\right), \quad (2)$$

where ρ_p and u_p are the density of liquid pentane and its molecular mass, respectively. r_o and r_i denote the radii of the outer and inner container walls, and t means time. The fit parameters h_1 and τ represent the increment of the surface level and the time scale of the absorption of the pentane vapor by the liquid toluene, respectively. We found $h_1 = 3.03 \pm 0.02 \times 10^{-3}$ m and $\tau = 895.0 \pm 7.3$ s.

A typical example for the time evolution of a wave train and the number of its wave crests is depicted in Fig. 2. At first, surface waves are generated. They are shown as a thin line in the diagram and were discussed in detail in [17]. From about 100 to 200 s there exists a periodic wave train. Its contrast in the shadowgraph image decreases until it fades away completely. At about 170 s appear very regular short waves, which can be considered as internal rather than surface waves as we shall clarify below. They are represented in the diagram by a thick line. From about 210 to 260 s there

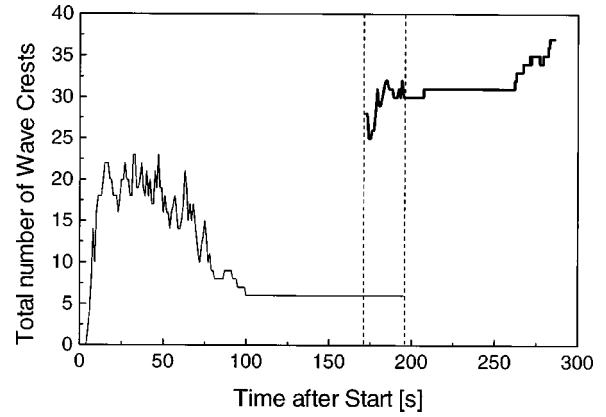


FIG. 2. Total number of waves in an experimental run as a function of time. The surface waves that are excited at the beginning are shown here as a thin line. At about 170 s, internal waves are generated as very regular short waves, represented in the diagram by a thick line. From about 210 to 260 s there exists a wave train of constant wave number. Finally, the contrast gets weaker and the number of crests increases until they are no longer observable. Inner diameter of the container 50 mm; $T = 298.55$ K.

exists a wave train of constant wave number. As time proceeds further, the number of crests increases and the contrast gets weaker until, finally, they are no longer observable.

B. Excitation of internal waves

The transition from surface to internal waves is shown in space-time diagrams in Fig. 3. The crests are visible as bright lines. Due to the periodic boundary condition, waves leaving the system on one side enter it on the other. Image (a) shows the transition from surface waves [19] to internal waves in an experimental run with the reservoir open to air. Here, the surface waves yield to internal waves of shorter wavelength. Later the gaps of low amplitude are filled with internal waves. Image (b) shows that the internal waves are generated behind the strong crests of three-dimensional surface waves [17]. At the beginning they experience strong damping but as time proceeds they survive while the surface waves disap-

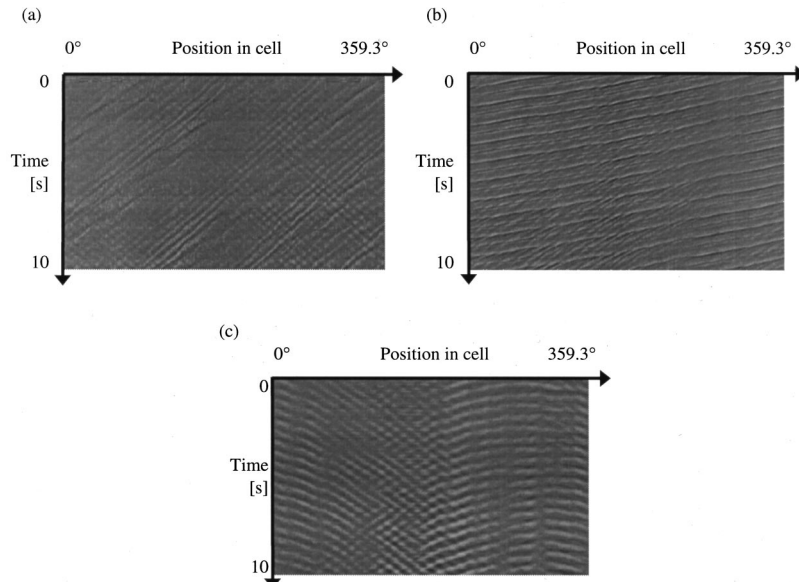


FIG. 3. Spatiotemporal diagrams of the generation of internal waves (a) by two-dimensional surface waves as reported in [19], (b) by three-dimensional surface waves discussed in [17], and (c) by a source of three-dimensional surface waves, also considered in [17]. (b) and (c) show experimental runs with a covered reservoir, (a) is with the reservoir open to the ambient air. The small internal waves in (b) are excited behind the strong crests of the surface waves. In (a), the internal waves are generated by contraction of the surface waves. Then they fill the gaps of low amplitude. In (c), the surface waves coming from a source change into internal waves on the way to the sink. In all cases, the strongest internal waves travel in the same azimuth direction as the surface waves. The inner diameter of (a) and (b) is 50 mm and of (c) 54 mm. Temperature (a): 299.75 K, (b) 298.55 K, (c) 297.95 K.

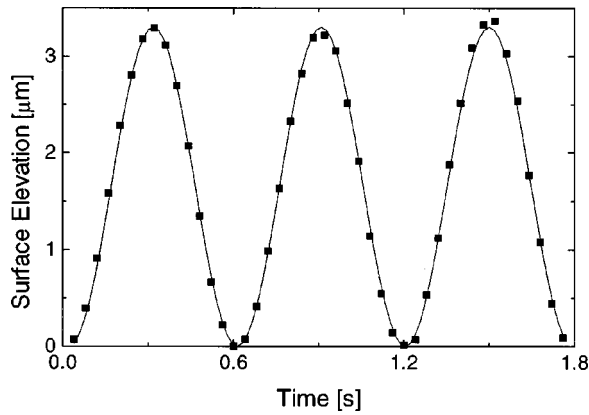


FIG. 4. Surface elevation of a train consisting of 20 internal waves with a sinusoidal fit to the data. $T=297.95$ K.

pear. The first internal waves observed in both situations [Figs. 3(a) and 3(b)] travel in the same direction as the surface waves. Later counter-rotating trains may also be excited. Surface waves coming from a “source” can also yield to internal waves. Image (c) of Fig. 3 displays this case. At the source, the surface waves slosh back and forth between the container walls. From there they invade the rest of the container and become radially aligned. While traveling, the surface waves slowly change their character, converting themselves into internal waves, which collide at the side opposite to the source.

C. Wave trains

The generated internal waves form trains that may rotate clockwise or counterclockwise. As expected due to symmetry, in a series of experiments both directions are observed with almost the same frequency. Two counter-rotating trains of different wave number have also been observed. The frequency f and wavelength λ are determined from spatiotemporal diagrams. The wavelength of the internal waves at the intermediate radius of the annular container with 54 mm inner diameter varies between 5.3 and 10.1 mm, which correspond to 38 and 20 wave crests, respectively. In the container with 50 mm inner diameter, trains consisting of 29–38 internal waves have been observed with a covered reservoir. During the experimental runs with the reservoir left open we detected trains of 20–32 waves. Thus, in the container of 50 mm inner diameter lower wave numbers are observed with an open reservoir and higher ones with a covered reservoir, while the entire wave number spectrum is excited in the container with 54 mm inner diameter. The mean frequency is determined as the number of wave crests divided by the time period of one complete cycle of a wave crest. The frequency of unmodulated wave trains increases linearly with time. It ranges between 1.6 and 2.6 Hz in the container of 54 mm inner diameter. In the other container the observed frequencies are generally higher and vary between 2.5 and 3.0 Hz. When left open to the ambient air the frequencies are between 1.5 and 2.1 Hz. The frequency of the internal waves increases significantly with the wave mode.

The internal waves cause a harmonic deformation at the surface in the azimuthal direction. The surface elevation, as detected with the reflected laser beam, can be fitted with a sinusoidal function as shown in Fig. 4. The surface deforma-

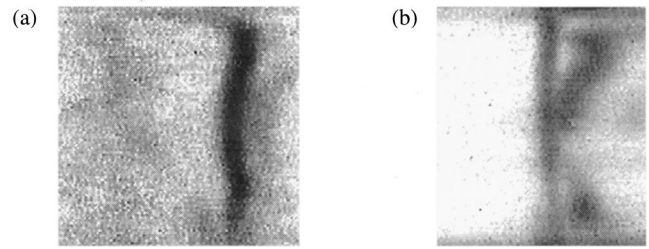


FIG. 5. Side view of the displaced column due to a train of 22 internal waves that travels to the left. Image (a) is taken 3.68 s after the exposure. In image (b) the column position 21.00 s after exposure has been overlaid with the column directly after exposure. The height of the side views is 9.3 mm and the widths are 9.3 and 8.0 mm, respectively. $T=299.75$ K.

tion induced by the internal waves amounts to only a few micrometers. The maximum surface amplitude as measured for the wave trains decreases with decreasing wavelength.

The flow visualization reveals that the internal waves produce a convective flow with only very small displacements of the colored column. Figure 5(a) shows a side view of the displaced column 3.68 s after irradiation. The image is taken while a train of 22 internal waves travels to the left. The dislocation of the colored column is undulated but the displacement is very small throughout the bulk. Only at the surface is there a strong drag in the direction of travel of the waves. A superposition of an image taken 21.00 s after irradiation on its original position is presented in Fig. 5(b). The signal close to the surface is no longer visible. But this image clearly reveals the net flow due to the internal waves. Together with the information from Fig. 5(a) we conclude that a slight surface layer moves in the travel direction of the waves while in the bulk the flow moves slowly in the opposite direction with a zone of almost zero horizontal velocity in the center region of the liquid layer. The horizontal velocity in the upper half of the layer is stronger than in the lower part.

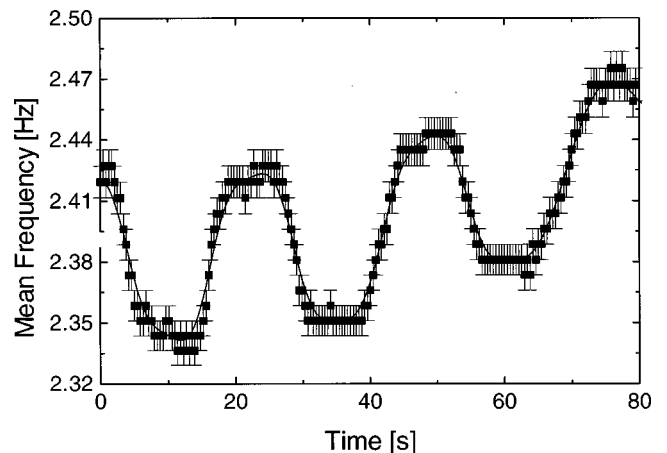


FIG. 6. Frequency of a modulated train of 30 waves as a function of time. The frequency is determined at a fixed position in the annular container as the mean frequency of one wave during one complete loop. Besides the long-time increase of frequency, it oscillates between extreme values. The oscillation travels with half the phase velocity. $T=298.05$ K.

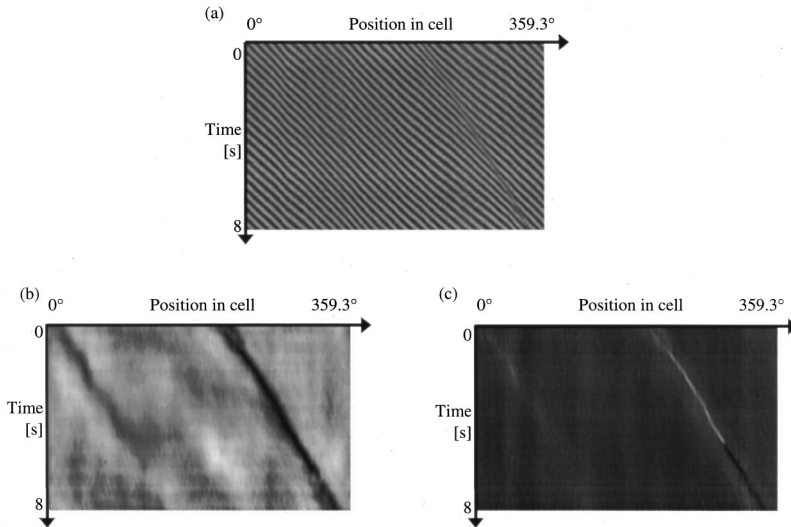


FIG. 7. Space-time diagram of a modulated train (a), its amplitude (b), and its wave number (c). The modulation, which is in the right half of the image, moves in the same direction as the waves. The intensity in the gray scale images (b) and (c) corresponds to the magnitude of the amplitude and wave number, respectively. The dark line in (c) corresponds to the low amplitude of the waves at the localized modulation. At the beginning there is a much higher wave number at the location of low amplitude than in the rest of the container. Later, this “quenched” wave disappears. This space-time point appears in (c) as a sharp intensity reversal. $T = 297.85$ K.

D. Modulations of wave trains

The internal wave trains show modulations. Figure 6 gives an example of the frequency oscillation in an internal wave train. At a fixed position in the annular container the modulations of the internal waves are apparently not damped. Besides its long-time increase, the frequency oscillates with an amplitude of up to 4% of the mean value. The modulations travel through the container with half the phase velocity.

Localized modulations lead to the disappearance or the creation of a single crest in a wave train. Figure 7(a) gives an example. A wave train with 31 crests shows a modulation that leads to the extinction of a single crest. Figures 7(b) and 7(c) display the amplitude of the shadowgraph contrast and the local wave number obtained from demodulation based on the method proposed in [20]. Their relative magnitudes are coded in gray values. Dark corresponds to low and light to high values. The amplitude is very low at the location of the modulation. At the beginning, the wave number is much higher at the location of low amplitude than in the rest of the container. It increases until one wave crest disappears. This space-time point appears in Fig. 7(c) as a sharp change of the gray value. When the wave disappears the amplitude decreases to noise level in the center of the modulation.

In addition to single localized modulations, we have observed several others of equal strength that coexist at the same time. Figure 8(a) displays a spatiotemporal diagram of a wave train with three pronounced modulations. Another example is shown in Fig. 8(b). In this case, two modulated wave trains counter-rotate at the same time. The train that

travels to the right has three low-amplitude regions and the left-traveling train has one. An interaction between the crossing modulations has not been observed.

Since the modulations are due to contributions in a narrow band of frequencies and thus move with the group velocity, they offer the possibility of determining the dispersion relation directly from single experimental runs, irrespective of the changes in absolute value from one experimental run to another with the change of the control parameter. Let ν be the ratio of phase and group velocity,

$$\nu = \frac{v_P}{v_G} = \frac{\omega/k}{d\omega/dk}, \quad (3)$$

where ω is the angular frequency, k the wave number, and v_P and v_G are the phase and group velocity, respectively. Then integration yields

$$\omega^\nu \propto k. \quad (4)$$

Figure 9 shows that the ratio of the wave's phase velocity and the velocity of the modulations is 2, independent of the wave number. Hence, the angular frequency is proportional to the square root of the wave number.

E. Pulses

As well as wave trains, we also observed narrow and extended pulses traveling through the container. They occur when a wave train dies out. The narrow pulses are made up of 5–7 waves and travel with a velocity about the group

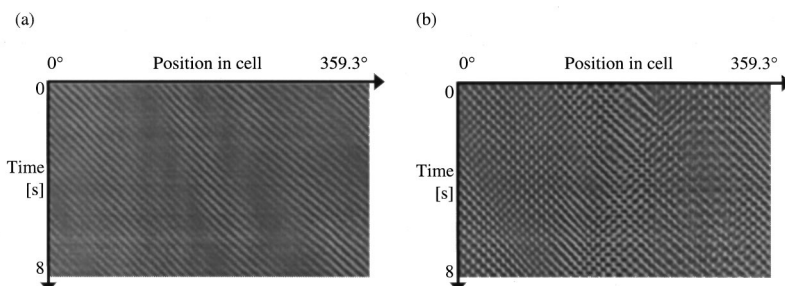


FIG. 8. Space-time diagrams of a wave train with several modulations. (a) shows one wave train with three modulations and (b) depicts two counter-rotating modulated wave trains. $T =$ (a) 297.75 K, (b) 297.65 K.

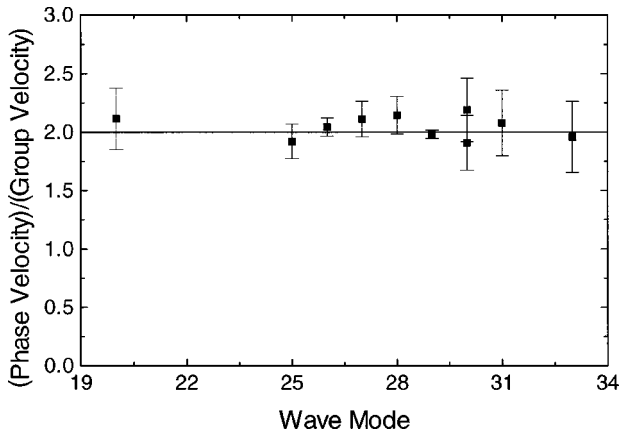


FIG. 9. Ratio between phase velocity and group velocity of the internal waves as a function of the wave mode. The ratio is determined for the modulations of the wave trains.

velocity of the underlying internal waves. They always occur at the end of an experimental run and are the last signs of convection. Figure 10(a) shows an example.

The extended pulses are observed earlier in the experimental runs, when the amplitude of the internal waves is still close to its maximum value. They usually come along with the generation of wave trains that travel in the opposite direction. As the amplitude of the wave train decreases, a small zone appears with increasing amplitude. Figure 10(b) shows an example of such a well developed region. A left-traveling wave train existed before and is disappearing. Outside a high-amplitude region the train has almost vanished while the high-amplitude domain travels through the container like a pulse. Its full width at half maximum (FWHM) is almost a quarter of the container circumference. Figure 10(c) depicts the amplitude for the time interval of image (b). As time goes on the high-amplitude region broadens and its amplitude slowly decreases. Finally, low-amplitude modulations set in and the pulse vanishes.

F. Oscillations between wave trains

The overall behavior of the amplitude and the wave number of an entire experimental run is given in Fig. 11. The

experimental run was carried out after five minutes from a former run. Surface waves are observed only during the first few seconds of the experimental run and are not depicted in Fig. 11. It shows the case where one wave train disappears in favor of a counter-rotating one. Figure 11(a) displays the amplitude and Fig. 11(b) the wave number. In both diagrams both right-traveling and left-traveling waves clearly appear. The noise level of the amplitude is about 2 units. For this reason only the wave numbers of waves with amplitudes above this threshold are shown.

At the beginning of the experimental run, waves traveling in both directions are excited. Their interaction pattern is not stationary since the counter-rotating trains have different wave numbers [see also Fig. 8(b)]. As time proceeds the left-traveling wave train, which has a higher wave number, dies out. Simultaneously, the amplitude of the right-traveling one increases although its wave number, which corresponds to 28 waves, remains unchanged. This holds also for the next period of amplitude decay. But in the final stage at weaker amplitude, modulations appear leading to an increase of the wave number. Then, in these modulations of weaker amplitude, left-traveling waves are generated. This results in an amplitude increase of the left-moving waves. The right-traveling train yields to the left-traveling one. After some modulations, the wave number of the new train remains constant, corresponding to 38 waves. Finally, the amplitude of the left-traveling train diminishes and the whole train disappears. At the end of this period, modulations appear and alter the wave number. During the coexistence of two counter-rotating wave trains at the beginning of the experimental runs, we have always observed energy transfer between the trains as the maximum amplitude oscillates between the wave trains.

IV. DISCUSSION

The internal waves are generated when the surface waves, which are generated at high surface stresses due to the Marangoni effect [17,19] during the absorption of pentane vapor by toluene, are already very weak and disappearing. Flow visualization reveals that the shear flow at the surface points in the travel direction of the waves and is stronger than the

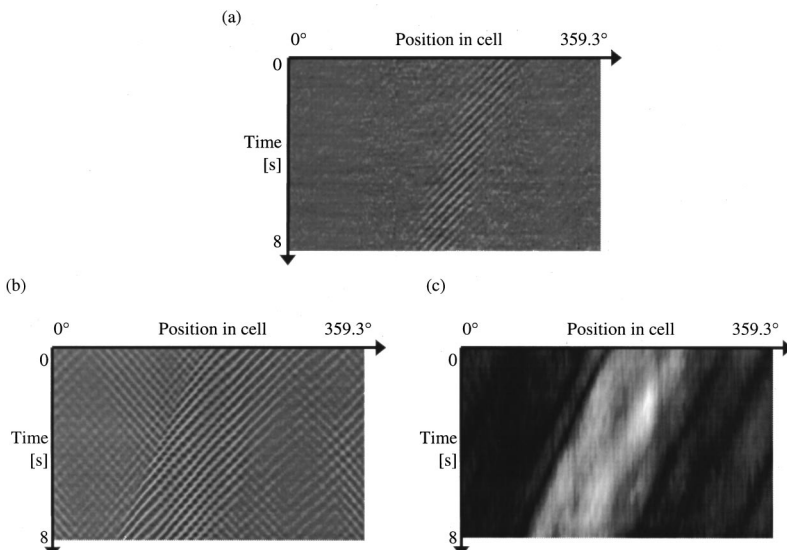


FIG. 10. Narrow and extended pulses. The contrast in (a) has been enhanced by about a factor of 4.5. (c) shows the amplitude of the left-moving waves train in (b). During the time interval presented here, the zone of high amplitude has a full width at half maximum (FWHM) of 49.5 ± 0.8 mm, which corresponds to a quarter of the container. $T = 297.95$ K.

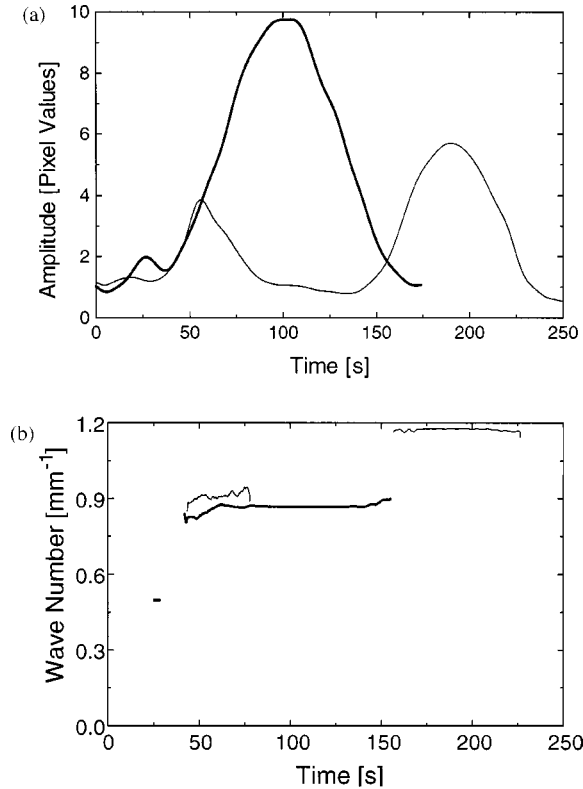


FIG. 11. Amplitude (a) and wave number (b) of internal waves during an experimental run. Surface waves that are excited during the first second are not shown. The thick and thin lines indicate the right-traveling and left-going trains, respectively. The noise level of the amplitude is about 2 units. The wave number is only shown for amplitudes beyond this threshold. At the beginning of the experimental run, waves that travel in both directions are excited. After a time of coexistence the left-traveling wave train dies out and the amplitude of the remaining right-moving train increases. Later on, its amplitude decreases again until it disappears in favor of a left-traveling one of higher wave number. $T = 297.85$ K.

convective flow in the liquid bulk beneath. It is apparently the driving shear of the internal waves. In the bulk the horizontal flow goes down to zero in the center of the bulk. The convection is asymmetric and stronger in the upper part of the liquid.

Even though there is still a strong shear flow at the surface, the waves are indeed internal waves. First of all, the convection profile in the bulk is typical for internal waves. Second, we found a dispersion relation typical for gravity waves. The amplitude of the sinusoidal surface deformation, however, is about $3 \mu\text{m}$ at most. The dispersion relation for gravity waves with a sharp interface reads

$$\omega = \left(\frac{\rho_1 - \rho_2}{\rho_1 + \rho_2} gk \right)^{1/2} = \left(\frac{(\rho_T - \rho_P)(C_2 - C_1)}{2\rho_T - (\rho_T - \rho_P)(C_2 + C_1)} gk \right)^{1/2}, \quad (5)$$

where ω , k , and g denote angular frequency, wave number, and gravitational acceleration, respectively. ρ_1 and ρ_2 and C_1 and C_2 are the densities and pentane concentrations in the lower and upper liquid layers, respectively, and ρ_T and ρ_P are the densities of toluene and pentane. We remark that this dispersion relation is also the limiting case for surface shear

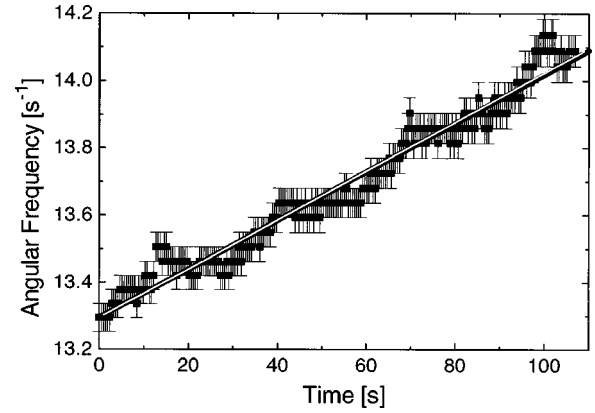


FIG. 12. Increase of angular frequency of a wave train. The linear fit to the experimental data is shown in black and a fit from the dispersion relation (5) is presented in white. The parameters are $C_1(t=0) = 0$, $C_2(t=0) = 0.152$, and $\Delta C_2 / \Delta C_1 = 1.12$.

induced by surface-tension changes. Comparing the measured frequencies to those expected for surface and internal waves reveals that the angular frequency of pure surface waves varies between 78 and 103 s^{-1} . For internal waves in a two-layer system of pure pentane over pure toluene the angular frequency is in the interval between 31 and 43 s^{-1} . The experimental values, however, range between 11 and 16 s^{-1} . This is clearly below the values for pure liquid layers. For the exact density values one needs to know the concentration distribution within the liquid. Since in the lower part of the liquid [17] there is hardly any convection accompanying the earlier generated surface waves, we may assume that the pentane concentration is very low if not zero in the lower layer, when the internal waves are generated. Thus, we may set the pentane concentration in the lower layer C_1 equal to zero and solve Eq. (5) for the upper concentration. For the measured frequencies and wave numbers we obtain a pentane concentration in the upper half of the liquid that varies from 0.125 to 0.180 in the container with 54 mm inner diameter, and concentrations between 0.170 and 0.211 in the container with 50 mm inner diameter. Calculating the average pentane concentration for the upper half of the liquid in the annular container with 50 mm inner diameter from the surface-level measurements, we get values of about 0.121 – 0.138 for the onset of internal waves. Even though the assumption of averaging over the strong stratification in the upper layer may seem very rough at first glance, this shows that the internal waves can be interpreted in a first approximation as those appearing in a two-layer system.

To maintain a constant frequency the concentration in the upper layer must increase like the density ratio of the layer with respect to the concentration in the lower layer:

$$\frac{\Delta C_2}{\Delta C_1} = \frac{\rho_2}{\rho_1}. \quad (6)$$

For the internal waves this lies in the narrow range between 0.95 and 0.96 . The experimental data with increasing frequency is fitted well with a ratio slightly larger than unity. Figure 12 presents an example. The linear fit to the frequency is in very good agreement with the fit from the dis-

persion relation at a ratio of 1.12 between the increment of the upper concentration and that of the lower one.

The shear flow at the surface is caused by surface stresses due to the absorption of the pentane (Marangoni effect). It works apparently in the same way as a shear flow within a two-layer liquid, a case long ago considered by Taylor [1] and Goldstein [2]. They described the instability of inviscid fluids which can be characterized by the Richardson number Ri , $Ri = \rho(dv/dz)^2[(d\rho/dz)g]^{-1}$, with ρ the density, v the horizontal velocity, and derivatives taken along the vertical coordinate. It is the ratio of the destabilizing shear to the stabilizing effect of the stable stratification (negative buoyancy). Here the adequate ratio of surface-tension-gradient-driven stresses to (negative) buoyancy is the parameter that should describe our experimental findings of internal waves. Actually, it can be interpreted as an (inverse) dynamic Bond number $Bo^* = (\Delta\rho)gd^2/(\Delta\sigma)$ with $(\Delta\rho)$ and $(\Delta\sigma)$ denoting, respectively, the variations of density and surface tension due to the surfactant concentration gradient. In the language of Bénard-like convection [12], this quantity $Bo^* = Ra/Ma$, where Ra is the Rayleigh number for buoyancy-driven convection (here negative) and Ma is the Marangoni number for surface-tension-gradient-driven convection (which also takes on negative values).

In a simplified two-layer model, the density variation can be taken as the difference between the average densities of the respective layers, and the height would be the liquid depth. The corresponding Marangoni number, whose explicit expression is not needed here, is determined in the same way as in [17] for surface waves. The Rayleigh number [12] here can be constructed in two ways. One may take the values of the concentration as determined from the dispersion relation (5) with the pentane concentration equal to zero in the lower layer at the beginning and the increment as fitted to data as in Fig. 12. In this case the buoyancy reads $(\rho_T - \rho_P)(C_2 - C_1)gh^3$. The other possibility consists in taking as the starting value the mean concentration obtained by measuring the surface level and then taking the increment from the fit. Taking into account the absolute uncertainties in determining all the parameters, we aim only for the order of magnitude of the characteristic number and its temporal evolution. Then Bo^* is about 10^{-8} and decreases by a factor of 1.5 while the internal waves are still observable.

The internal waves show all the ingredients of a short-wave instability. As time goes on, Bo^* decreases and the wave number increases, showing that there exists a finite wave number at bifurcation. During the experimental runs, the number of waves in a train usually increases as time proceeds. The wave number changes always happen by localized modulations that travel through the container with the phase velocity. Only frequencies in a very narrow band contribute to these modulations. This is typical for the Eckhaus instability, where one wave number becomes unstable and yields to a neighboring wave number. An experimental observation of the Eckhaus instability in traveling-wave systems has been reported by Janiaud *et al.* [21] in a Rayleigh-Bénard experiment with an additional lateral temperature difference. Later on it was further investigated by Kolodner in wave trains occurring in buoyancy-driven convection with binary fluid mixtures [22]. In both cases the wave amplitude

was found to decrease strongly in the center of the localized modulation, as we have observed it for our internal waves.

Using a Ginzburg-Landau framework, Janiaud *et al.* [21] found numerically that various modulations should be observable in extended systems, i.e., where the length of the system is much longer than the wavelength. However, their experimental system with 6–12 waves in the annular container was too small to observe this. The waves in Kolodner's experiment have a nonmonotonic dispersion relation [22]. Therefore, he could observe forward and backward traveling modulations in his extended system with 38–43 waves. We have observed several wave train modulations at the same time, as predicted in [21]. Because of their dispersion relation they all travel in the forward direction. Counter-rotating modulations also exist during the coexistence of counter-rotating wave trains. As in Kolodner's experiment [22], our experiment also showed that counter-rotating modulations do not cancel each other, but a mutual influence could not be found.

Further evidence of the Eckhaus instability is the frequency modulation, as shown in Fig. 6. At a fixed position, the frequency of the wave train oscillates around the slowly increasing mean frequency. This oscillation moves through the container at half the phase velocity. Thus, it is a beat of two frequencies that correspond to two neighboring wave numbers. The same kind of oscillation, although for a constant control parameter, were observed for traveling waves by Kolodner [22]. In that experiment the oscillations set in for a certain wave number after exceeding a suitable value of the control parameter. Decreasing the control parameter resulted in a decrease of the growth rate of the oscillation. This growth rate could be set to zero at a certain value of the control parameter when decreasing the control parameter, while there was no oscillation when the control parameter was increased to the same value. This fact revealed the subcriticality of the bifurcation. Although we cannot control the inverse Bond number in our experiment, the frequency oscillations suggest that the bifurcation into internal waves is subcritical.

Evidence of this subcritical bifurcation is obtained from the observation of pulses. Pulses indeed exist in the bistable range of systems with a subcritical bifurcation. In this regime a part of the system is in the lower, generally the homogeneous state and another part, the pulse, is on the bifurcated branch. We have observed narrow and extended pulses. In accordance with pulses found in binary fluid mixtures [23,24], the narrow pulses occur at the end of the experimental runs, when the inverse Bond number is lowest. The extended pulses are observed at an earlier stage of the run, indicating that the subcriticality of the bifurcation into internal waves is quite pronounced.

We have often observed the coexistence of two counter-rotating wave trains. In general, these trains have different wave numbers. The wave pattern indicates that they interact with each other in a weakly nonlinear manner. Even though there is only one wave train excited at the beginning, another counter-rotating one may be generated thereafter. The amplitude maxima usually oscillate between the two counter-rotating trains. The reversal of the travel direction may be due to a detuning between the bulk motion governed by the

dispersion relation of the internal waves and the surface shear governed by the Marangoni effect. Although the shorter waves are excited by surface-tension stresses, they travel according to *their* dispersion relation. Note that where the pentane is absorbed the surface tension decreases and the surface is stretched. The absorbed pentane, on the other hand, lowers the actual absorption rate. When it is not carried away fast enough from the place where it was adsorbed it hinders the surface there from absorbing. This may lead to an asymmetry of the surface tension along each wave crest, which accumulates as time proceeds. Then surface stresses (the Marangoni effect) tend to reverse and surface motion tends to develop more and more in the direction opposite to that of the traveling wave and may, finally, provoke its over-

turn and, consequently, a counter-traveling train develops in full.

ACKNOWLEDGMENTS

The authors acknowledge fruitful discussions with Professor Yu. S. Ryazantsev, Dr. P. Colinet, Dr. A. Ye. Rednikov, Dr. Julia Rees, and Dr. W. B. J. Zimmerman. They also thank Professor Elvira Rodenas and her collaborators for permitting measuring the surface tension with their Lauda tensiometer. A.W. gratefully acknowledges financial support by the Gottlieb Daimler- und Karl Benz-Stiftung. This research was supported by the Spanish Ministry of Education and Culture under Grant Nos. PB93-81 and PB96-599, and by the European Union under ICOPAC Grant No. UE-HPRN-CT-2000-00136.

-
- [1] G. I. Taylor, Proc. R. Soc. London, Ser. A **132**, 499 (1931).
 [2] S. Goldstein, Proc. R. Soc. London, Ser. A **132**, 524 (1931).
 [3] J. W. Miles, J. Fluid Mech. **10**, 496 (1961).
 [4] J. W. Miles, J. Fluid Mech. **16**, 209 (1963).
 [5] P. Hazel, J. Fluid Mech. **51**, 39 (1972).
 [6] P. G. Drazin, Proc. Cambridge Philos. Soc. **58**, 646 (1962).
 [7] B. D. Dore, J. Fluid Mech. **40**, 113 (1970).
 [8] S. A. Thorpe, J. Fluid Mech. **32**, 489 (1968).
 [9] S. A. Thorpe, J. Fluid Mech. **46**, 299 (1971).
 [10] J. W. Miles, J. Fluid Mech. **3**, 185 (1957).
 [11] F. K. Ball, J. Fluid Mech. **19**, 465 (1964).
 [12] A. Ye. Rednikov, P. Colinet, M. G. Velarde, and J. C. Legros, J. Fluid Mech. **405**, 57 (2000).
 [13] *CRC Handbook of Chemistry and Physics*, 76th ed., edited by D. R. Lide (CRC, West Palm Beach, FL, 1996).
 [14] C. R. Wilke and C. Y. Lee, Ind. Eng. Chem. **47**, 1253 (1955).
 [15] *Chemical Engineers' Handbook*, 5th ed., edited by R. H. Perry and C. H. Chelton (Mc Graw-Hill, New York, 1973).
 [16] J. Kendall and K. P. Monroe, J. Am. Chem. Soc. **39**, 1787 (1917).
 [17] A. Wierschem, M. G. Velarde, and H. Linde, J. Colloid Interface Sci. **212**, 365 (1999).
 [18] V. N. Yurechko and Yu. S. Ryazantsev, Exp. Therm. Fluid Sci. **1**, 1 (1991).
 [19] H. Linde, M. G. Velarde, A. Wierschem, W. Waldhelm, K. Loeschcke, and A. Y. Rednikov, J. Colloid Interface Sci. **188**, 16 (1997).
 [20] P. Kolodner and H. Williams, in *Nonlinear Evolution of Spatio-Temporal Structures in Dissipative Continuous Systems*, Vol. 225 of *NATO Advanced Study Institute*, edited by F. H. Busse and L. Kramer (Plenum, New York, 1990), pp. 73–91.
 [21] B. Jانياud, A. Pumir, D. Bensimon, V. Croquette, H. Richter, and L. Kramer, Physica D **55**, 269 (1992).
 [22] P. Kolodner, Phys. Rev. A **46**, 6431 (1992).
 [23] P. Kolodner, Phys. Rev. E **50**, 2731 (1994).
 [24] W. Barten, M. Lücke, and M. Kamps, Phys. Rev. Lett. **66**, 2621 (1991).